







Capturing the ground state of uranium dioxide from first principles: Crystal distortion, magnetic structure, and phonons

Shuxiang Zhou ¹, Hao Ma ², Enda Xiao ³, Krzysztof Gofryk,¹ Chao Jiang,¹ Michael E. Manley ²,
David H. Hurley ¹ and Chris A. Marianetti ⁴

¹*Idaho National Laboratory, Idaho Falls, Idaho 83415, USA*

²*Oak Ridge National Laboratory, Oak Ridge, Tennessee 37831, USA*

³*Department of Chemistry, Columbia University, New York, New York 10027, USA*

⁴*Department of Applied Physics and Applied Mathematics, Columbia University, New York, New York 10027, USA*



(Received 5 May 2022; revised 8 August 2022; accepted 9 September 2022; published 20 September 2022)

Uranium dioxide (UO₂) remains a formidable challenge for first-principles approaches due to the complex interplay among spin-orbit coupling, Mott physics, magnetic ordering, and crystal distortions. Here we use DFT+*U* to explore UO₂ at zero temperature, incorporating all the aforementioned phenomena. The technical challenge is to navigate the many metastable electronic states produced by DFT+*U*, which is accomplished using *f*-orbital occupation matrix control to search for the ground state. We restrict our search to the high-symmetry ferromagnetic phase, including spin-orbit coupling, which produces a previously unreported occupation matrix. This newfound occupation matrix is then used as an initialization to explore the broken symmetry phases. We find the oxygen cage distortion of the 3k antiferromagnetic state to be in excellent agreement with experiments, and both the spin-orbit coupling and the Hubbard *U* are critical ingredients. We demonstrate that only select phonon modes have a strong dependence on the Hubbard *U*, whereas magnetic ordering has only a small influence overall. We perform measurements of the phonon dispersion curves using inelastic neutron scattering, and our calculations show good agreement when using reasonable values of *U*. The quantitative success of DFT+*U* warrants exploration of thermal transport and other observables within this level of theory.

DOI: [10.1103/PhysRevB.106.125134](https://doi.org/10.1103/PhysRevB.106.125134)

I. INTRODUCTION

Uranium dioxide (UO₂) has attracted a great deal of research interest ever since the 1950s, given its use as a standard nuclear fuel. The partially filled *f* shell in uranium sets the stage for rich physics, and extensive experiments have characterized the behavior of UO₂. At ambient temperature and pressure, UO₂ crystallizes in the fluorite structure with a lattice parameter of 5.47 Å [1], and exhibits paramagnetism [2,3]. Upon cooling, UO₂ undergoes an antiferromagnetic (AFM) transition at $T_N = 30.8$ K [4], and there is a concomitant oxygen cage distortion whereby the oxygen ions move 0.014 Å from their fluorite positions along the ⟨111⟩ directions [5] (see Fig. 1 of Ref. [6] for a schematic, in addition to further details). More specifically, the antiferromagnetism is a noncollinear 3k ordering [7–10], which is aligned with the oxygen cage distortion.

Extensive first-principles calculations were also performed on UO₂, and here we focus on ground state properties. It is well known that UO₂ is incorrectly predicted to be metallic when using density functional theory (DFT) within conventional approximations to the exchange-correlation energy, including the local density approximation (LDA) and generalized gradient approximation (GGA), due to their failure to describe the strong correlation of the 5*f* electrons of uranium. Going beyond conventional DFT, various approaches have been developed to better capture the effects of strong

local interactions; these approaches include hybrid functionals [11–13], self-interaction correction [14,15], DFT+*U* [16,17], and DFT plus dynamic mean-field theory (DMFT) [18,19]. Although all these approaches predict UO₂ to be an insulator, DFT+*U* is the most widely used, thanks to its simplicity and relatively low computational cost. Furthermore, DFT+*U* shares a degree of overlap with all the aforementioned techniques. DFT+*U* is recovered from DFT+DMFT when solving the DMFT impurity problem within Hartree-Fock [19], DFT+*U* can be viewed as a local hybrid functional [20], and the DFT+*U* functional is general enough to account for self-interaction corrections. Given that DFT+*U* relies on a Hartree-Fock-like approximation, it must break symmetry and strongly polarize the system in order to offer a reasonable description of energetics when dealing with strong interactions. Therefore, DFT+*U* brings challenges to modeling UO₂, given the large number of possible spin and orbital orderings in the case of 5*f* electrons. Indeed, many metastable states are found when performing DFT+*U* on UO₂, and some calculated properties (e.g., the band gap) are highly dependent on the exact ordered state [21].

Multiple methods have been designed to search for the ground state in DFT+*U*, including occupation matrix control (OMC) [21–24], the quasi-annealing scheme [25], and the *U*-ramping method [26], all of which have been applied to UO₂. None of these schemes can guarantee that the ground state will be found, and different research efforts using these

different methods have, in practice, generated different results. For example, both Thompson *et al.* [27] and Wang *et al.* [28] used the U -ramping method and found 1k AFM ground states with different occupation matrices. Earlier work by Laskowski *et al.* [29] and Gryaznov *et al.* [30], which did not elaborate on how the ground state search was performed, found 3k AFM ground states with significantly larger oxygen cage distortions (0.16 and 0.09 Å, respectively). Dorado *et al.* [6] and Thompson *et al.* [28] employed OMC and the U -ramping method, respectively, and both found a lowest-energy structure with 1k AFM ordering. The only study that found a 3k AFM ground state featuring oxygen cage distortion on the same scale as the experiments was Zhou *et al.* [24] (i.e., 0.024 Å), who used an OMC technique based on inputs from crystal field calculations, along with a different type DFT+ U functional.

Phonons may serve as a delicate probe of the electronic structure, and are a key ingredient in thermal transport. As such, a large number of experimental studies [31–34] and DFT-based computational studies [34–40] have been performed on UO_2 . While different first-principles methods have successfully captured various aspects of the phonon dispersion curves and elastic constants, large discrepancies still exist. For example, the predicted phonon frequency of the highest longitudinal optical mode, denoted LO2 [34], at the L point (0.5, 0.5, 0.5) varies from 50 [38] to 70 meV [39]. More details on the discrepancies of previous DFT+ U calculations of phonons as compared with experiments are reviewed in Supplemental Material (SM)[41]. These discrepancies might be attributable to various differences in the calculations, such as the value of U , the magnetic ordering, and whether or not spin-orbit coupling (SOC) was included. Furthermore, even for calculations performed under the exact same theory, there is no guarantee that the different researchers converged upon the same ground state, which potentially yields different phonons. Indeed, very few previous studies report details on their obtained UO_2 ground state (e.g., the uranium f -electron occupation matrices), making it extremely challenging to reproduce prior work and understand the origin of discrepancies.

In this DFT+ U study of UO_2 , we perform a ground state search using OMC within the ferromagnetic (FM) state, both with and without SOC, yielding a previously unreported occupation matrix. Our new ground state is then used as the starting point for exploring states with further broken symmetries, yielding unprecedented agreement with experiments. Given this new understanding, we then explore the elastic constants and phonon dispersion curves, comparing the phonons with new inelastic neutron scattering data and untangling the various roles of U , magnetic ordering, and SOC.

II. COMPUTATIONAL DETAILS

Our DFT calculations were carried out using the projector augmented-wave (PAW) method [42,43], as implemented in the Vienna *ab initio* Simulation Package (VASP) code [44,45]. Two exchange correlation functionals were employed: LDA and GGA as formulated by Perdew, Burke, and Ernzerhof (PBE) [46]. A plane-wave cutoff energy of 550 eV was used, and the energy convergence criterion was 10^{-8} eV. The Hub-

bard correction was included in the LDA+ U or GGA+ U approximation to account for the strong local interactions of the uranium f electrons. Specifically, we used the simplified rotationally invariant DFT+ U approach from Dudarev *et al.* [47], which only employs a single effective interaction. We customized the VASP code to monitor and impose the occupation matrices during the calculation [41]. The calculated states were controlled via two methods. First, specific occupation matrices were imposed during the first several electronic steps, and then the calculation was allowed to proceed self-consistently without constraint (i.e., OMC). Second, a specific charge density was used to initialize a calculation—a process we refer to as charge density initialization. Symmetry was turned off for all calculations.

Above T_N , the space group of UO_2 is $Fm\bar{3}m$ and the point group symmetry of the uranium site is O_h . For FM calculations, the primitive cell of UO_2 was used and a $13 \times 13 \times 13$ Monkhorst-Pack k -point mesh [48] was applied; for AFM calculations, the conventional cubic cell was used and a $7 \times 7 \times 7$ Monkhorst-Pack k -point mesh was applied. The phonons and elastic constants were calculated via the lone irreducible derivative (LID) approach [49]. LID uses central finite difference to individually compute each group's theoretically irreducible derivative in the smallest possible supercell, minimizing the possibility of numerical inadequacies. Finite difference displacement amplitudes of 0.01, 0.02, 0.03, and 0.04 Å were used to construct quadratic error tails, ensuring that the discretization error is properly accounted for. The face-centered cubic lattice vectors are encoded in a 3×3 row stacked matrix $\hat{\mathbf{a}} = \frac{a_0}{2}(\hat{\mathbf{J}} - \hat{\mathbf{I}})$, where $\hat{\mathbf{I}}$ is the identity matrix and $\hat{\mathbf{J}}$ is a matrix in which each element is 1. The Brillouin zone is discretized using a real space supercell $\hat{\mathbf{S}}_{BZ}\hat{\mathbf{a}}$, where $\hat{\mathbf{S}}_{BZ}$ is an invertible matrix of integers which produces superlattice vectors that satisfy the point group [49]. In this study, all irreducible derivatives corresponding to $\hat{\mathbf{S}}_{BZ} = 2\hat{\mathbf{S}}_C$ were obtained, where $\hat{\mathbf{S}}_C$ generates the conventional cubic cell and is defined as $\hat{\mathbf{S}}_C = (\hat{\mathbf{J}} - 2\hat{\mathbf{I}})$. The supercell $2\hat{\mathbf{S}}_C$ has a multiplicity of 32 and therefore contains 96 atoms; though the LID approach allows one to extract all of the irreducible derivatives from supercells that have multiplicity 4 (i.e., 12 atoms) or less. In the case of 1k and 3k AFM, the magnetism breaks the symmetry of the $Fm\bar{3}m$ space group, and therefore we use a primitive unit cell of $\hat{\mathbf{S}}_C\hat{\mathbf{a}}$, which is commensurate with both 1k and 3k. When computing phonons for 1k and 3k, we discretize the Brillouin zone using $\hat{\mathbf{S}}_{BZ} = 2\hat{\mathbf{I}}$, meaning that all irreducible derivatives consistent with the AFM supercell $2\hat{\mathbf{S}}_C$ will be extracted. In order to best compare with the experiment, we also unfold the AFM phonon band structure back to the original primitive unit cell $\hat{\mathbf{a}}$, averaging any translational symmetry breaking. The Born effective charges ($Z_U^* = 5.54$ and $Z_O^* = -2.77$) of the U and O ions and the dielectric constant ($\epsilon = 5.69$) were used to account for LO-TO splitting [50,51].

III. GROUND STATE SEARCH FOR UO_2

Determining the ground state of UO_2 within DFT+ U is very complex, and exploring all of the phase space is not tractable. Our approach consists of three different stages, all executed using GGA. For stage 1, we used OMC for a given

TABLE I. States of FM UO_2 with SOC, as found in stage 2 of our ground state search. The results are sorted by increasing relative energy, with respect to the fully relaxed crystal having occupation matrix S_0 and energy E_{\min} .

State	Degeneracy	Initialized from States	$E_{\text{und}} - E_{\min}$ (meV/ UO_2)	$E_{\text{dis}} - E_{\min}$ (meV/ UO_2)	Strain Distortion ($\epsilon_{xx}, \epsilon_{yy}, \epsilon_{zz}, \epsilon_{xy}, \epsilon_{xz}, \epsilon_{yz}$) $\times 10^3$	Oxygen Cage Distortion
S_0	1	$S_0, S_1, S_2, S_4, S_5, S_6, S_8$	0.3	0	(-1, -1, 2, 0, 0, 0)	-
S_1	2	S_2, S_4, S_7	68.9	67.7	(-5, 2, 3, 0, 0, 0) ^a	-
S_2	4	S_1, S_2	72.3	70.8	(-4, 5, 0, 0, 0, 0) ^a	-
S_3	1	S_3	72.9	71.5	(-3, -3, 5, 0, 0, 0)	-

^aSymmetry-equivalent states are given in the Supplemental Material [41].

trial occupation matrix and performed computations in the FM state without SOC. For stage 2, the charge density from the stage 1 results was used to initialize a FM calculation with SOC. For stage 3, we used OMC with the resulting stage 2 occupation matrix, and performed an AFM calculation with SOC. Stage 1 was executed for a large number of trial occupation matrices (see below for details), while stage 2 was only executed for the low-energy subset of the stage 1 results. Stage 3 was only executed for the lowest-energy state of stage 2. All the calculations evaluated two types of structural relaxations: relaxing only the volume of the structural cubic crystal (denoted as the undistorted crystal), and full structural relaxations that may break the symmetry (denoted as the distorted crystal).

For stage 1, we followed Dorado *et al.*'s works [6,21] and used randomly generated diagonal and nondiagonal occupation matrices (221 and 900 matrices, respectively) as trials. The nine lowest energies we found (denoted as S_0 - S_8 , with S_0 having the lowest energy) consisted of 25 distinct occupation matrices, some of which were related by symmetry. Details on this search process and the selected properties of the 25 states, including occupation matrices, can be found in SM [41]. Our lowest-energy class of states, S_0 , contains an orbital ordering that induces structural symmetry breaking via a pure shear strain ($\pm 0.017 T_{2g}$ mode), further lowering the energy by 10 meV relative to the relaxed cubic structure. The S_1 class is 13 meV higher in energy than the S_0 class, and one occupation matrix within S_1 is what Dorado *et al.* found to be the lowest-energy state in their search. Therefore, we have found a lower energy state within our search, though there is no guarantee that even lower-energy states do not exist. However, the shear strain distortion associated with the S_0 class of states is not observed in the experiments. This discrepancy is not particularly problematic, given that SOC will favor a different occupation matrix.

A. Ferromagnetism with SOC

Previous work reported that SOC may have important impacts on phonons [52]. However, the role of SOC in influencing the ground state occupation matrix of UO_2 has not been carefully explored. Therefore, we now proceed to our stage 2, in which the low-energy subset of results from stage 1 are used to initialize FM calculations that include SOC. The results of stage 2 are given in Table I, comparing both the relative energy and the distortion. In regard to the energy, the nine lowest-energy classes found without SOC converge into four lowest-energy classes when using SOC, and the relative

energies between the classes are significantly changed. For example, the calculation initialized by one state in S_2 ended up in S_3 with the highest energy, while the calculation initialized by higher-energy state S_8 ended up in S_0 . Furthermore, calculations initialized from degenerate states within the same class sometimes converged to different classes when using SOC: The six degenerate states in S_2 converged to S_0 , S_1 , and S_2 . It is clear that SOC significantly perturbs the system. SOC also changes the strain distortions. For example, a T_{2g} strain exists in S_0 , S_3 , S_6 , and S_8 , but not in any of the reported SOC states. The same trend holds for the oxygen cage distortion (compare Table I to Table S1 in SM [41]).

Stage 2 of our ground state search resulted in a lowest-energy state S_0 (see SM [41], Sec. I.D.1) that was substantially lower than all the others. Interestingly, the S_0 state is also found without using OMC (i.e., initializing the calculation in the default manner), which might be reasonable given that it is so much lower in energy than S_1 . It should be noted that S_0 has no appreciable strain, thus there are no immediate inconsistencies with experiments. Although there is no oxygen cage distortion for S_0 , we will demonstrate that magnetic ordering will generate such distortions.

B. AFM UO_2 with SOC

In stage 3, we used S_0 to initialize the $1\mathbf{k}$ and $3\mathbf{k}$ AFM calculations performed using GGA+ U with $U = 4$ eV. These results were then used to initialize GGA+ U for other U values in addition to LDA+ U calculations. We found that, for each magnetic order, the converged occupation matrix of LDA+ U was approximately the same as the occupation matrix of GGA+ U (see SM [41] Sec. I.E).

For $U = 4$ eV, the energies, lattice parameters, and distortions of UO_2 for each magnetic order are given in Table II. GGA+ U predicts a lattice parameter 0.08 Å larger than the experiment, while LDA+ U is 0.02 Å smaller. For both LDA+ U and GGA+ U , the FM and $1\mathbf{k}$ AFM order have a nonzero E_g strain mode, while the $3\mathbf{k}$ AFM order has no nonzero strains; and the latter is consistent with experiments. Alternatively, for both LDA+ U and GGA+ U , neither the FM nor $1\mathbf{k}$ AFM order has an oxygen cage distortion, whereas the $3\mathbf{k}$ AFM has an oxygen cage distortion with an amplitude of 0.016 Å in the $\langle 111 \rangle$ -type direction; which is in good agreement with the experimental result of 0.014 Å. Therefore, we see that the $3\mathbf{k}$ AFM order is a necessary condition for achieving the oxygen cage distortion along the $\langle 111 \rangle$ direction. Furthermore, the $3\mathbf{k}$ AFM order is stable even in the absence of the oxygen cage distortion, indicating magnetism

TABLE II. Energies and distortions calculated for different magnetic structures and functionals at $U = 4$ eV with SOC: FM, 1k AFM, and 3k AFM, as computed using LDA+ U and GGA+ U .

Potential	Magnetic Structure	$E_{\text{und}} - E_{\text{dis}}^{3k}$ (meV/ UO_2)	$E_{\text{dis}} - E_{\text{dis}}^{3k}$ (meV/ UO_2)	Lattice Parameters (\AA)	Strain Distortion ($\epsilon_{xx}, \epsilon_{yy}, \epsilon_{zz}, \epsilon_{xy}, \epsilon_{xz}, \epsilon_{yz}$) $\times 10^3$	Oxygen Cage Distortion
LDA+ U	FM	20.0	17.7	5.450	(-1, -1, 2, 0, 0, 0)	-
LDA+ U	1k AFM	8.6	8.4	5.450	(0, -1, 1, 0, 0, 0)	-
LDA+ U	3k AFM	1.3	0	5.450	-	(111) 0.016 \AA
GGA+ U	FM	0.4	0.1	5.546	(-1, -1, 2, 0, 0, 0)	-
GGA+ U	1k AFM	-3.7	-3.9	5.546	(0, -1, 1, 0, 0, 0)	-
GGA+ U	3k AFM	1.0	0	5.547	-	(111) 0.016 \AA

to be the dominant energy scale and the oxygen cage distortion acts cooperatively. LDA+ U predicts the 3k AFM order to be the lowest in energy, while GGA+ U predicts the 1k AFM to be lowest and the 3k AFM and FM are essentially degenerate. Overall, for the above set of experimental observables, LDA+ U appears to be in better agreement with the experiments than is GGA+ U .

We now study how the results depend on U . Figure 1 shows the energies of FM and 1k AFM relative to the 3k AFM, including oxygen cage distortions. Neither LDA+ U nor GGA+ U show any qualitative changes over this range. The GGA+ U results are rather insensitive to U , while the FM state in LDA+ U changes rather strongly. The lattice parameter and oxygen cage distortion are shown in Fig. 2. The lattice parameter increases with U in both cases, and LDA+ U agrees better with experimental results at $U = 4$ eV, given that it generated a large underprediction at $U = 0$, as expected. The oxygen cage distortion is largest at $U = 1$ eV and decreases with increasing U . Coincidentally, the LDA+ U and GGA+ U results happen to cross at approximately $U = 4$ eV.

It is important to make comparisons with previous calculations whenever possible, and we attempted to reproduce the

3k AFM states and corresponding large oxygen cage distortions reported by Laskowski *et al.* (0.16 \AA) [29] and Gryaznov *et al.* (0.09 \AA) [30] with GGA+ U +SOC. However, we were unable to reproduce any of these findings, highlighting the complexity of performing DFT+ U in correlated f electron systems, and illustrating why explicit reporting of the occupation matrix is critical. Interestingly, the S_0 state in the 1k AFM structure is found without using OMC (i.e., initializing the calculation in the default manner), while this was not the case for the 3k AFM structure.

IV. PHONONS

Based on the lowest-energy state S_0 , the elastic constants and phonon dispersion curves were calculated via the LID approach [49] using DFT+ U +SOC calculations. The elastic constants calculated with $U = 4$ eV for the FM, 1k AFM, and 3k AFM states are presented in Table III, in addition to Brandt *et al.*'s low temperature results for the 3k AFM state [32]. All of the magnetic states have small structural distortions which

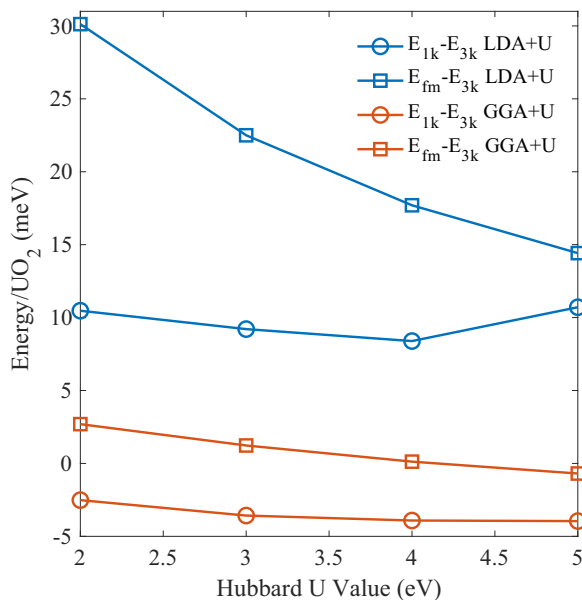


FIG. 1. Calculated energy difference of distorted UO_2 for FM and 1k AFM relative to 3k AFM using LDA+ U and GGA+ U with SOC, as a function of the Hubbard U .

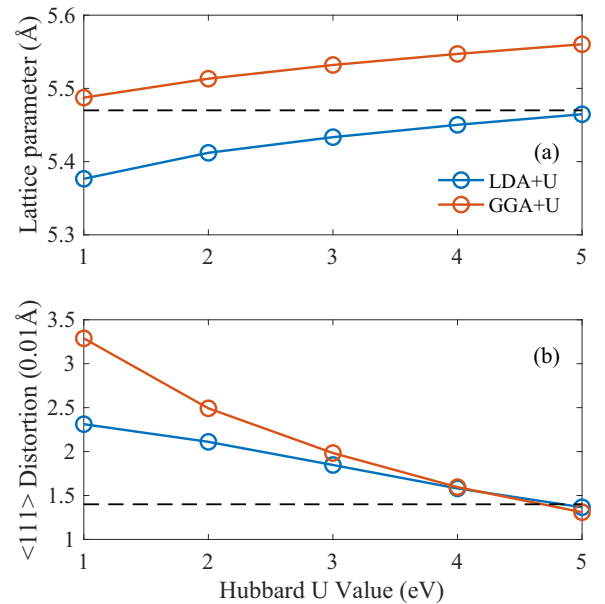


FIG. 2. Calculated (a) lattice parameter and (b) $\langle 111 \rangle$ oxygen cage distortion in the 3k AFM state, using LDA+ U +SOC and GGA+ U +SOC, as a function of the Hubbard U . The horizontal dashed lines represent the experimental values of the lattice parameter from Idiri *et al.* [1] and the distortion from Santini *et al.* [3].

TABLE III. Calculated elastic constants based on the lowest-energy FM and AFM states, using DFT+ U ($U = 4$ eV) with SOC, in addition to experimental results at 10 K from Brandt *et al.* [32].

	C_{11} (GPa)	C_{12} (GPa)	C_{44} (GPa)
Brandt <i>et al.</i> [32]	400	125	59
LDA+ U : FM	394.8	136.2	78.7
LDA+ U : 1k AFM	398.8	131.8	78.5
LDA+ U : 3k AFM	394.4	132.0	77.8
GGA+ U : FM	358.4	113.0	60.8
GGA+ U : 1k AFM	379.8	120.1	62.0
GGA+ U : 3k AFM	380.1	119.7	62.6

break O_h symmetry (see Table II), but the deviation is very small in all cases. Therefore, we use C_1 symmetry and average the elastic constants to restore O_h symmetry (see Table III), and the unaveraged results are in SM (see SM [41] Sec. II G). We find that magnetic ordering has essentially no influence on the LDA+ U results, and only a small influence in the case of GGA+ U . Neither LDA+ U nor GGA+ U is in perfect agreement with the experiments, though the GGA+ U results fall within a 10% margin of error. Furthermore, by using $U = 5$ eV in LDA+ U for the 3k AFM state, the calculated elastic constants are $(C_{11}, C_{12}, C_{44}) = (387, 138, 78)$ GPa, which are very close to the $U = 4$ eV values, meaning that the acoustic phonon properties are approximately saturated at $U = 4$ eV.

We now consider the unfolded phonon dispersion curves of \mathbb{S}_0 in the 3k AFM state (see Section II E in SM [41] for additional details), using LDA+ U +SOC and GGA+ U +SOC ($U = 4$ eV), and compare against the experimental phonon dispersion curves from Pang *et al.* at 300 K [34], the density of states from Bryan *et al.* at 10 K [53], the phonon dispersion curves at 600 K from this work, and the density of states at 77 K from this work (see Fig. 3). Generally, the GGA+ U results are in better agreement with experiments for all phonon branches except the highest frequency one (LO2). In the original work by Pang *et al.* [34], the LO2 mode fit could not have accounted for Bryan *et al.*'s later discovery of an anharmonic feature appearing just above the phonons [54], which probably explains the additional scatter toward higher frequencies in their fit points as compared to ours. Interestingly, many of the differences between LDA+ U and GGA+ U are attributable to the difference in lattice parameter (see SM [41] Sec. II B).

We now explore the effect of magnetic ordering and the Hubbard U on the unfolded phonon dispersion curves. Comparing the phonons for the FM, 1k AFM, and 3k AFM states when using GGA+ U +SOC ($U = 4$ eV) (see Fig. 4), there are only small differences, demonstrating that magnetic ordering only has a minor effect on the quadratic portion of the vibrational Hamiltonian. The symmetry breaking in the FM and 1k AFM states is large enough to be noticed visually, but still very small (though see Fig. S7 [41] for plots along additional directions where splittings are more pronounced). Alternatively, the Hubbard U does have a strong effect on select phonon branches, as demonstrated by computing the phonon dispersion curves of \mathbb{S}_0 in the 3k AFM state, using GGA+ U +SOC [see Fig. 5(a)]. All acoustic phonon branches are approximately independent of the Hubbard U , while two

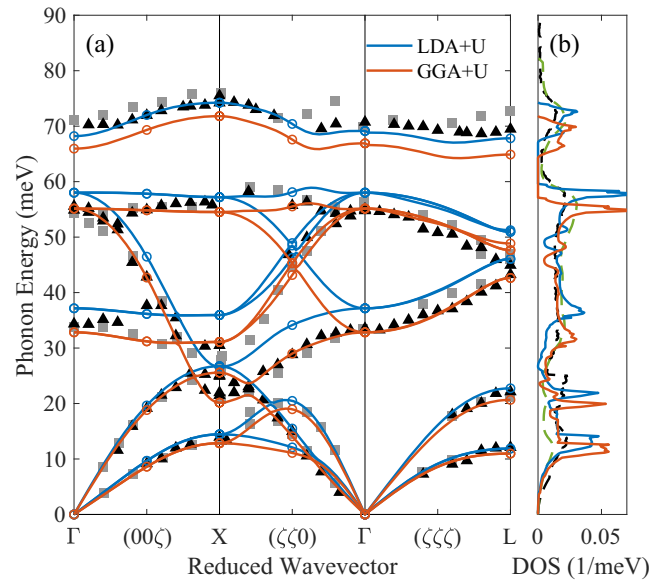


FIG. 3. Phonons of 3k AFM UO_2 . (a) The unfolded phonon dispersion curves and (b) density of states of LDA+ U +SOC and GGA+ U +SOC ($U = 4$ eV) (solid lines), compared with inelastic neutron scattering data from Pang *et al.* [34] at 300 K (grey squares), this work at 600 K (black triangles), this work at 77 K (dashed black curves), and Bryan *et al.* [53] at 10 K (dashed green curves). The hollow points were directly computed using DFT+ U , while the corresponding lines are Fourier interpolations.

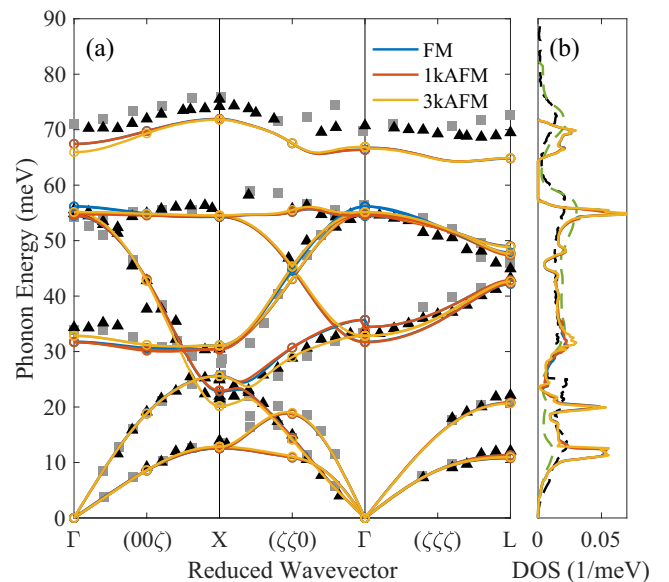


FIG. 4. Phonons of UO_2 in different magnetic states. (a) The GGA+ U +SOC ($U = 4$ eV) phonon dispersion of FM and unfolded dispersion of 1k AFM and 3k AFM, and (b) density of states, compared with inelastic neutron scattering data from Pang *et al.* [34] at 300 K (grey squares), this work at 600 K (black triangles), this work at 77 K (dashed black curves), and Bryan *et al.* [53] at 10 K (dashed green curves). The hollow points were directly computed using DFT+ U , while the corresponding lines are Fourier interpolations.

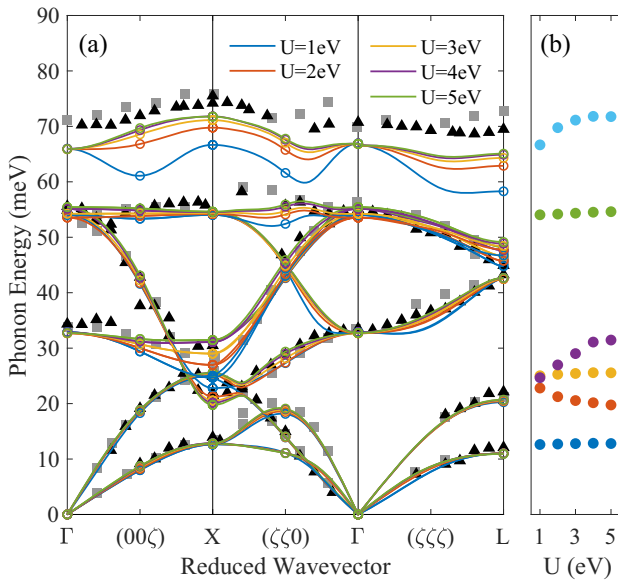


FIG. 5. (a) Unfolded phonon dispersion (solid curves) and (b) phonon frequencies at the X point (filled points), calculated for $3\mathbf{k}$ AFM UO_2 using $\text{GGA}+U+\text{SOC}$, as functions of the Hubbard U . In panel (a), the phonon dispersion are compared with inelastic neutron scattering data from Pang *et al.* [34] at 300 K (grey squares), and from this work at 600 K (black triangles). The hollow points were directly computed using $\text{DFT}+U$, while the corresponding lines are Fourier interpolations. In panel (b), the different colors represent different phonon modes at X point.

optical phonon branches, TO1 and LO2, are significantly affected by the Hubbard U . More specifically, the phonon frequencies of the TO1 and LO2 branches at X points [see Fig. 5(b)], along with the LO2 branch at L points, increase with increasing U . However, the U dependence eventually saturates, as indicated by the small difference between $U = 4$ and $U = 5$ eV.

V. CONCLUSION

In summary, we investigated the ground state properties of UO_2 by using $\text{DFT}+U$, including SOC. Particular emphasis was placed on searching for the ground state occupation matrix, and this was executed in the FM state using $U = 4$ eV. When incorporating SOC, we found a previously unreported occupation matrix \mathbb{S}_0 that we then used to extensively explore the symmetry-broken phases, where the resulting occupation matrices are closely related to \mathbb{S}_0 . When exploring the $3\mathbf{k}$ AFM state, we found an oxygen cage distortion that was in excellent agreement with experimental results. Both the

Hubbard U and SOC, along with the concomitant occupation matrix \mathbb{S}_0 , are necessary for obtaining the $3\mathbf{k}$ AFM state and the oxygen cage distortion. Furthermore, including the Hubbard U in the absence of SOC results in a spurious shear strain distortion that is not observed in experiment.

Both LDA and GGA were explored in our $\text{DFT}+U$ calculations, and each appears to offer some particular advantage in describing the known experimental outcomes. As expected, at $U = 0$, LDA underpredicts and GGA overpredicts the lattice constant, and an increasing U increases the lattice parameter in both cases, yielding better agreement for $\text{LDA}+U$ at $U = 4$ eV. Both functionals accurately predict the oxygen cage distortion for a sufficiently large value of U (i.e., $U = 4$ eV). For the magnetic structure, $\text{LDA}+U$ correctly predicts the $3\mathbf{k}$ AFM state to be lower in energy than the $1\mathbf{k}$ AFM and FM states, while $\text{GGA}+U$ incorrectly predicts the $1\mathbf{k}$ AFM to be lower in energy than the $3\mathbf{k}$ AFM state. That being said, these energy differences are all on a small scale and should be treated with caution. Phonons were extensively explored: only selected modes have a nontrivial dependence on U , and magnetic ordering only has a small influence. At $U = 4$ eV, both LDA and GGA give reasonable results, though LDA better describes the LO2 mode (albeit showing some deficiency with the TO1/LO1 modes), whereas GGA gives the opposite result. Most of these differences are attributable to the difference in lattice constant between LDA and GGA. In summary, $\text{DFT}+U$ offers a quantitatively reasonable picture of UO_2 , as compared to experiments. The success of $\text{DFT}+U$ in describing the ground state properties of UO_2 warrants exploration of finite temperature properties, including thermal conductivity.

ACKNOWLEDGMENTS

This work is supported by the Center for Thermal Energy Transport under Irradiation, an Energy Frontier Research Center funded by the U.S. Department of Energy (DOE) Office of Basic Energy Sciences. This research used resources at the Spallation Neutron Source, a DOE Office of Science User Facility operated by the ORNL. This research made use of Idaho National Laboratory computing resources, which are supported by the DOE Office of Nuclear Energy and the Nuclear Science User Facilities under Contract No. DE-AC07-05ID14517. This research also used resources of the National Energy Research Scientific Computing Center, a DOE Office of Science User Facility supported by the Office of Science of the U.S. Department of Energy under Contract No. DE-AC02-05CH11231. The phonon unfolding was supported by Grant No. DE-SC0016507 funded by the U.S. Department of Energy, Office of Science.

- [1] M. Idiri, T. Le Bihan, S. Heathman, and J. Rebizant, *Phys. Rev. B* **70**, 014113 (2004).
- [2] G. H. Lander, J. Faber, A. J. Freeman, and J. P. Desclaux, *Phys. Rev. B* **13**, 1177 (1976).
- [3] P. Santini, S. Carretta, G. Amoretti, R. Caciuffo, N. Magnani, and G. H. Lander, *Rev. Mod. Phys.* **81**, 807 (2009).

- [4] W. M. Jones, J. Gordon, and E. A. Long, *J. Chem. Phys.* **20**, 695 (1952).
- [5] J. Faber, G. H. Lander, and B. R. Cooper, *Phys. Rev. Lett.* **35**, 1770 (1975).
- [6] B. Dorado, G. Jomard, M. Freyss, and M. Bertolus, *Phys. Rev. B* **82**, 035114 (2010).

- [7] P. Burel, J. Rossat-Mignod, S. vuevel, O. Vogt, J. C. Spirlet, and J. Rebivant, *J. Less-Common Met. Proceedings of Actinides 85, Aix en Provence - Part I*, **121**, 121 (1986).
- [8] K. Ikushima, S. Tsutsui, Y. Haga, H. Yasuoka, R. E. Walstedt, N. M. Masaki, A. Nakamura, S. Nasu, and Y. Ōnuki, *Phys. Rev. B* **63**, 104404 (2001).
- [9] E. Blackburn, R. Caciuffo, N. Magnani, P. Santini, P. J. Brown, M. Enderle, and G. H. Lander, *Phys. Rev. B* **72**, 184411 (2005).
- [10] S. B. Wilkins, R. Caciuffo, C. Detlefs, J. Rebizant, E. Colineau, F. Wastin, and G. H. Lander, *Phys. Rev. B* **73**, 060406 (2006).
- [11] K. N. Kudin, G. E. Scuseria, and R. L. Martin, *Phys. Rev. Lett.* **89**, 266402 (2002).
- [12] I. D. Prodan, G. E. Scuseria, and R. L. Martin, *Phys. Rev. B* **76**, 033101 (2007).
- [13] A. D. Becke, *J. Chem. Phys.* **98**, 1372 (1993).
- [14] L. Petit, A. Svane, Z. Szotek, W. M. Temmerman, and G. M. Stocks, *Phys. Rev. B* **81**, 045108 (2010).
- [15] J. P. Perdew and A. Zunger, *Phys. Rev. B* **23**, 5048 (1981).
- [16] S. L. Dudarev, D. N. Manh, and A. P. Sutton, *Philos. Mag. B* **75**, 613 (1997).
- [17] V. I. Anisimov, J. Zaanen, and O. K. Andersen, *Phys. Rev. B* **44**, 943 (1991).
- [18] A. Georges, G. Kotliar, W. Krauth, and M. J. Rozenberg, *Rev. Mod. Phys.* **68**, 13 (1996).
- [19] G. Kotliar, S. Y. Savrasov, K. Haule, V. S. Oudovenko, O. Parcollet, and C. A. Marianetti, *Rev. Mod. Phys.* **78**, 865 (2006).
- [20] L. A. Agapito, S. Curtarolo, and M. Buongiorno Nardelli, *Phys. Rev. X* **5**, 011006 (2015).
- [21] B. Dorado, B. Amadon, M. Freyss, and M. Bertolus, *Phys. Rev. B* **79**, 235125 (2009).
- [22] B. Amadon, F. Jollet, and M. Torrent, *Phys. Rev. B* **77**, 155104 (2008).
- [23] G. Jomard, B. Amadon, F. Bottin, and M. Torrent, *Phys. Rev. B* **78**, 075125 (2008).
- [24] F. Zhou and V. Ozoliņš, *Phys. Rev. B* **83**, 085106 (2011).
- [25] H. Y. Geng, Y. Chen, Y. Kaneta, M. Kinoshita, and Q. Wu, *Phys. Rev. B* **82**, 094106 (2010).
- [26] B. Meredig, A. Thompson, H. A. Hansen, C. Wolverton, and A. van de Walle, *Phys. Rev. B* **82**, 195128 (2010).
- [27] J. Wang, R. C. Ewing, and U. Becker, *Phys. Rev. B* **88**, 024109 (2013).
- [28] A. E. Thompson and C. Wolverton, *Phys. Rev. B* **84**, 134111 (2011).
- [29] R. Laskowski, G. K. H. Madsen, P. Blaha, and K. Schwarz, *Phys. Rev. B* **69**, 140408 (2004).
- [30] D. Gryaznov, E. Heifets, and D. Sedmidubsky, *Phys. Chem. Chem. Phys.* **12**, 12273 (2010).
- [31] I. J. Fritz, *J. Appl. Phys.* **47**, 4353 (1976).
- [32] O. G. Brandt and C. T. Walker, *Phys. Rev. Lett.* **18**, 11 (1967).
- [33] G. Dolling, R. A. Cowley, and A. D. B. Woods, *Can. J. Phys.* **43**, 65 (1965).
- [34] J. W. L. Pang, W. J. L. Buyers, A. Chernatynskiy, M. D. Lumsden, B. C. Larson, and S. R. Phillpot, *Phys. Rev. Lett.* **110**, 157401 (2013).
- [35] Q. Yin and S. Y. Savrasov, *Phys. Rev. Lett.* **100**, 225504 (2008).
- [36] A. J. Devey, *J. Nucl. Mater.* **412**, 301 (2011).
- [37] M. Sanati, R. C. Albers, T. Lookman, and A. Saxena, *Phys. Rev. B* **84**, 014116 (2011).
- [38] Y. Yun, D. Legut, and P. M. Oppeneer, *J. Nucl. Mater.* **426**, 109 (2012).
- [39] B.-T. Wang, P. Zhang, R. Lizárraga, I. Di Marco, and O. Eriksson, *Phys. Rev. B* **88**, 104107 (2013).
- [40] G. Kaur, P. Panigrahi, and M. C. Valsakumar, *Modell. Simul. Mater. Sci. Eng.* **21**, 065014 (2013).
- [41] See Supplemental Material at <http://link.aps.org/supplemental/10.1103/PhysRevB.106.125134> for information about UO₂ states found in our ground state search, phonon spectra of selected states, VASP patch files for OMC, and experimental details about inelastic neutron scattering. See also Refs. [55–57].
- [42] P. E. Blöchl, *Phys. Rev. B* **50**, 17953 (1994).
- [43] G. Kresse and D. Joubert, *Phys. Rev. B* **59**, 1758 (1999).
- [44] G. Kresse and J. Hafner, *Phys. Rev. B* **47**, 558 (1993).
- [45] G. Kresse and J. Furthmüller, *Phys. Rev. B* **54**, 11169 (1996).
- [46] J. P. Perdew, K. Burke, and M. Ernzerhof, *Phys. Rev. Lett.* **77**, 3865 (1996).
- [47] S. L. Dudarev, G. A. Botton, S. Y. Savrasov, C. J. Humphreys, and A. P. Sutton, *Phys. Rev. B* **57**, 1505 (1998).
- [48] H. J. Monkhorst and J. D. Pack, *Phys. Rev. B* **13**, 5188 (1976).
- [49] L. Fu, M. Kornbluth, Z. Cheng, and C. A. Marianetti, *Phys. Rev. B* **100**, 014303 (2019).
- [50] M. A. Mathis, A. Khanolkar, L. Fu, M. S. Bryan, C. A. Dennett, K. Rickert, J. M. Mann, B. Winn, D. L. Abernathy, M. E. Manley, D. H. Hurley, and C. A. Marianetti, *Phys. Rev. B* **106**, 014314 (2022).
- [51] X. Gonze and C. Lee, *Phys. Rev. B* **55**, 10355 (1997).
- [52] B. Dorado, M. Freyss, B. Amadon, M. Bertolus, G. Jomard, and P. Garcia, *J. Phys.: Condens. Matter* **25**, 333201 (2013).
- [53] M. S. Bryan, J. W. L. Pang, B. C. Larson, A. Chernatynskiy, D. L. Abernathy, K. Gofryk, and M. E. Manley, *Phys. Rev. Mater.* **3**, 065405 (2019).
- [54] M. S. Bryan, L. Fu, K. Rickert, D. Turner, T. A. Prusnick, J. M. Mann, D. L. Abernathy, C. A. Marianetti, and M. E. Manley, *Commun. Phys.* **3**, 217 (2020).
- [55] D. L. Abernathy, M. B. Stone, M. J. Loguillo, M. S. Lucas, O. Delaire, X. Tang, J. Y. Y. Lin, and B. Fultz, *Rev. Sci. Instrum.* **83**, 015114 (2012).
- [56] J. W. L. Pang, A. Chernatynskiy, B. C. Larson, W. J. L. Buyers, D. L. Abernathy, K. J. McClellan, and S. R. Phillpot, *Phys. Rev. B* **89**, 115132 (2014).
- [57] A. I. Liechtenstein, V. I. Anisimov, and J. Zaanen, *Phys. Rev. B* **52**, R5467 (1995).